Supplementary Information for

Generating one-dimensional plasmonic arrays by laser-driven self-organization

Yilong Zhou[1,+], Quan Jiang[1,+], Xiaoqin Wu[1,*], Chunyan Zhu[1], Zhengyang Shen[1], Yuquan Miao[1], Lingxiao He[1], Liwen Xu[1], Yu-Cheng Chen[2], Yipei Wang[1,*], and Yi Xu[1]

[1] Key Laboratory of Optoelectronic Technology & Systems (Ministry of Education), College of Optoelectronic Engineering, Chongqing University, Chongqing 401331, China

[2] School of Electrical and Electronics Engineering, Nanyang Technological University, Singapore, Singapore.

[+]These authors contributed equally to this work.

* xiaoqinwu@cqu.edu.cn

* wangyp@cqu.edu.cn

1. Numerical models for electromagnetic fields on Ag nanowires (NWs)

An electromagnetic scattering study is carried out to simulate the field patterns using a finite element method (FEM) performed by COMSOL Multiphysics. Specifically, a plane *p*-polarized electromagnetic wave (λ = 490 nm) is incident on an Ag NW (D = 90 nm) on a prism substrate (n_s = 1.46) under total internal reflection. The dielectric constants of Ag are taken from COMSOL libraries. The surrounding medium is air (n_a = 1). In the model, a full field is first simulated for the plane wave obliquely incident on the silica-air interface with the NW absent, and then use it as a background field to calculate the scattered field with the NW present.

2. Parameters for the theoretical model

To determine the parameters in Eq.1-3 in the manuscript, we export the scattered E_y and E_z field, as well as k_{sp}, α, r, δ, ω, L from COMSOL simulation results, and then fit them with Eq. (4), which returns us the fitting algorithm information, including the parameters involving with the amplitude information (A, B, η_y, η_z) and the phase information (φ_{sp}, φ_y, φ_z). Table 1 list the parameter values for a Ag NW length with setting L = 12 μm and laser fluence = 20 mJ cm^{-2}. It can be seen that, $|\varphi_y-\varphi_z| < 1.1$ holds at a broad θ range of 50-85°, indicating the phase difference is appreciably small to be neglected.

	A	$B\eta_y/A$	$B\eta_z/A$	φ_y	φ_z	φ_{sp}	$\lvert\varphi_y-\varphi_z\rvert$
50 deg	1.81159E7	1.69061	0.93007	-0.54125	-1.61872	-0.39181	1.07747
55 deg	1.98847E7	1.29648	0.78154	2.01027	0.94737	2.08018	1.0629
60 deg	2.17003E7	1.04147	0.64228	-1.22339	-2.25676	-1.2287	1.03337
65 deg	2.29785E7	0.81739	0.49566	2.35806	1.37552	2.33766	0.98254
70 deg	2.40078E7	0.65833	0.37118	0.29641	-0.61966	0.25065	0.91607
75 deg	2.36984E7	0.53165	0.25679	-1.16233	-1.98622	-1.20917	0.82389
80 deg	2.19144E7	0.44073	0.1423	-1.87219	-2.31199	-1.90005	0.4398
85 deg	1.6332E7	0.37577	0.0984	-1.87282	-2.22832	-1.85064	0.3555

Table S1. Key parameter values returned after fitting the electric fields for a Ag NW.

3. Determine the thermal conductivity *k* of Ag NWs

The thermal conductivity k of Ag NWs is crucial to calculate the final spatial temperature distribution. For metal NWs, the surface-to-volume ratio is large and the scattering from the grain boundaries are significant, making the thermal conductivity distinct from the bulk materials.

According to the Lu model [1] and taking account into the Kapitza resistance term[2], the thermal conductivity k of Ag NW can be written as

$$k=\frac{k_{\mathrm{b}}\left(\frac{E_{\mathrm{n}}}{E_{\mathrm{b}}}\right)^{\frac{5}{2}}\frac{\left(T_{\mathrm{Mb}}-T_0\right)}{\left[T_{\mathrm{Mb}}\frac{E_{\mathrm{n}}}{E_{\mathrm{b}}}-T_0\right]}}{1+\frac{R_{\mathrm{k}}k_{\mathrm{b}}}{D}\left(\frac{E_{\mathrm{n}}}{E_{\mathrm{b}}}\right)^{\frac{5}{2}}\frac{\left(T_{\mathrm{Mb}}-T_0\right)}{\left[T_{\mathrm{Mb}}\left(\frac{E_{\mathrm{n}}}{E_{\mathrm{b}}}\right)-T_0\right]}} \tag{1}$$

where k_{b} is the thermal conductivity of bulk materials (for Ag, k_{b} = 424 W K^{-1} m^{-1}), E_{n} and E_{b} denote the cohesive energy for nanomaterial and bulk material, T_{Mb} is the melting temperature of bulk materials (for Ag, T_{Mb} = 1235.15 K), T_0 is the reference temperature (T_0 = 300 K in our case), R_{k} represents the Kapitza resistance, and D is the diameter of NW. In Eq.1, the cohesive energy ratio $E_{\mathrm{n}}/E_{\mathrm{b}}$ can be expressed as[2]

$$\frac{E_{\mathrm{n}}}{E_{\mathrm{b}}}=\left(1-\frac{1}{2D/D_0-1}\right)\exp\left(\frac{-2\lambda S_{\mathrm{b}}}{3R}\frac{1}{\left(D/D_0\right)-1}\right) \tag{2}$$

where S_{b} stands for the vibrational entropy (for Ag, S_{b} = 104.7 J mol^{-1} K^{-1} [1]), R = 8.31432 J mol^{-1} K^{-1} is the universal gas constant, and λ represents the shape factor whose value varies according to different shapes (for NWs, λ = 1). D_0 is defined as the critical diameter at which the maximum number of atoms are located on the surface, and it can be described as[2]

$$D_0=2(3-d)*h \tag{3}$$

where d is the degree of freedom (for NWs, d = 1), h indicates the atomic diameter (for Ag, h

= 0.289 nm [1]).

Once the NW's diameter is known, the cohesive energy ratio E_n/E_b can be obtained through Eq. 2. By substituting Eq.2 into Eq.1 and as long as the value of R_k is known, the thermal conductivity k can be derived. Previous studies have shown that the thermal conductivity k of a 147-nm-diameter Ag NW is 64.8 W K^{-1} m^{-1} [3]. In this case, via fitting the k value with Eq.1, we can obtain $R_k = 1.865\times10^{-9}$ K m^2 W^{-1}. Results show that, R_k can be defined as the temperature jump ΔT across an interface subject to a constant flowing heat flux J (i.e., $R_k = \Delta T/J$), and the value of R_k can be considered the same for nanostructures with similar sizes [4]. So, we substitute D = 90 nm and the R_k value into Eq.1, and get the thermal conductivity k = 42.3 W K^{-1} m^{-1} in our case.

4. Boundary conditions for the heat transfer model

For numerical calculation, the outmost boundary condition (BC) is described as [5]

$$\vec{n}\cdot(-k\nabla T) = h(T - T_r) + \varepsilon\sigma(T^4 - T_r^4) \quad (4)$$

where T_r is set to be the room temperature 300 K, $\vec{n}$ is an outward vector perpendicular to the boundary, h is convection heat transfer coefficient, ε is surface emissivity, and $\sigma = 5.67\text{x}10^{-8}$ W m^{-2} K^{-4}) is the Stefan-Boltzmann constant. $\vec{n}\cdot(-k\nabla T)$ represents the outward conductive heat flux, which equals to the sum of convective heat flux and radiation heat flux. For the outmost air boundary, only the convective heat flux exits, so h = 5 W m^{-2} K^{-1}) is adopted. For the outmost silica boundary, due to the low thermal conductivity of silica (k = 1.38 W K^{-1} m^{-1}), most of the heat concentrate on the region near to the NW. As a result, on the outmost silica boundary, we have $T \approx T_r$, indicating the convective heat flux can be neglected. Thus, we can only consider the radiation heat flux, and for silica, the surface emissivity ε = 0.79 is adopted. All the internal BCs are set as continuous conditions.

5. Experimental methods for fabricating plasmonic arrays

A commercial supercontinuum white light source (SuperK COMPACT) was used to generate nanosecond laser pulses in a wavelength range of 450-2400 nm and with a pulse duration of ~2 ns. The repetition rate can be internally tuned from 1 Hz to 20 kHz to control the laser ablation speed. The laser fluence can be tuned in a range of 0-12.9 mJ cm^{-2} (corresponding to 0-6.4 MW cm^{-2}) by a continuously variable neutral density filter. With a 50 mm focal distance achromatic lens (Edmund #47637, optimal transmission range 425-675 nm), the laser pulses were loosely focused into an elliptical spot with a size of 100x40 μm. Commercially available silver NWs (XFNANO, XFJ05) with average diameters of 90 nm and lengths of 20-60 μm were dispersed on the substrate for fabricating nanoparticle arrays. For metals, the strong light absorption particularly in the violet or blue spectrums results in significant heat generation in the laser-excited volume [6]. In experiments, we compare the ablation effect of the pulsed laser light with wavelength λ < 500 nm and λ > 500 nm. As shown in Fig. S1, for the same laser fluence, the laser light with λ < 500 nm can easily ablate the horizontally aligned NWs into

nanoparticle arrays (Fig. S1a), while the laser light with $\lambda > 500$ nm seldomly ablate the NWs (Fig. S1b). The result proves that the blue band ($\lambda < 500$ nm) of the SC laser plays an important role in producing nanoparticles arrays from NWs. Thus, we consider the pulsed laser with an effective wavelength range of 450-500 nm.

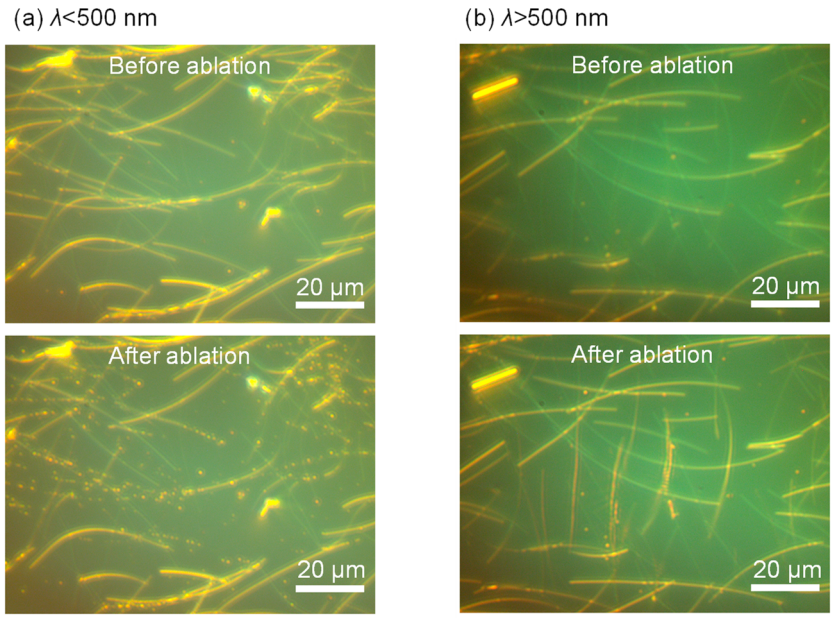

Fig. S1. (a) By inserting a 500-nm-shortpass filter after the supercontinuum nanosecond pulsed laser, the blue band ($\lambda < 500$ nm) of the laser was used to ablate the NWs. A variety of horizontally aligned NWs (up panel) were decomposed into nanoparticle arrays (bottom panel). (b) By inserting a 500-nm-longpass filter after the pulsed laser, the main visible band ($\lambda > 500$ nm) of the laser was used to ablate the NWs. Very few NWs were transformed into nanoparticle array.

6. Surface qualities of Ag NPs in the arrays

To characterize the surface roughness and defects of the Ag NPs fabricated by laser-driven self-organization, high-resolution scanning electron microscopy (SEM) was performed for the plasmonic array shown in Fig. S2a. Prior to SEM, to image the NPs fabricated on the silica prism, a conductive Au film was coated on the sample via sputtering. Fig. S2b shows typical high-magnification SEM images of the individual Ag NPs, exhibiting well-defined spherical shapes and relatively smooth surfaces. Note that, few small white spots observed around Ag NPs are attributed to nanometer-scaled Au grains formed during the sputtering of conductive films. To verify it, high-resolution SEM was also carried out for a Ag NW on the same prism but without laser ablation (Fig. S3a), where white spots with similar sizes were also found on the surfaces and the peripheries. As a control group, we also imaged the Ag NWs on a conductive Si substrate without Au sputtering under the same SEM imaging parameters, and the white spots were not observed on the NW surface (Fig. S3b). By comparison between Fig. S3a and Fig. S3b, it can be concluded that the white spots on the surface of the Ag NPs mainly come from the Au sputtering. Apart from the white spots, the Ag NP surfaces appear relatively smooth, without any obvious irregularities, indicating the NPs are free from noticeable surface defects.

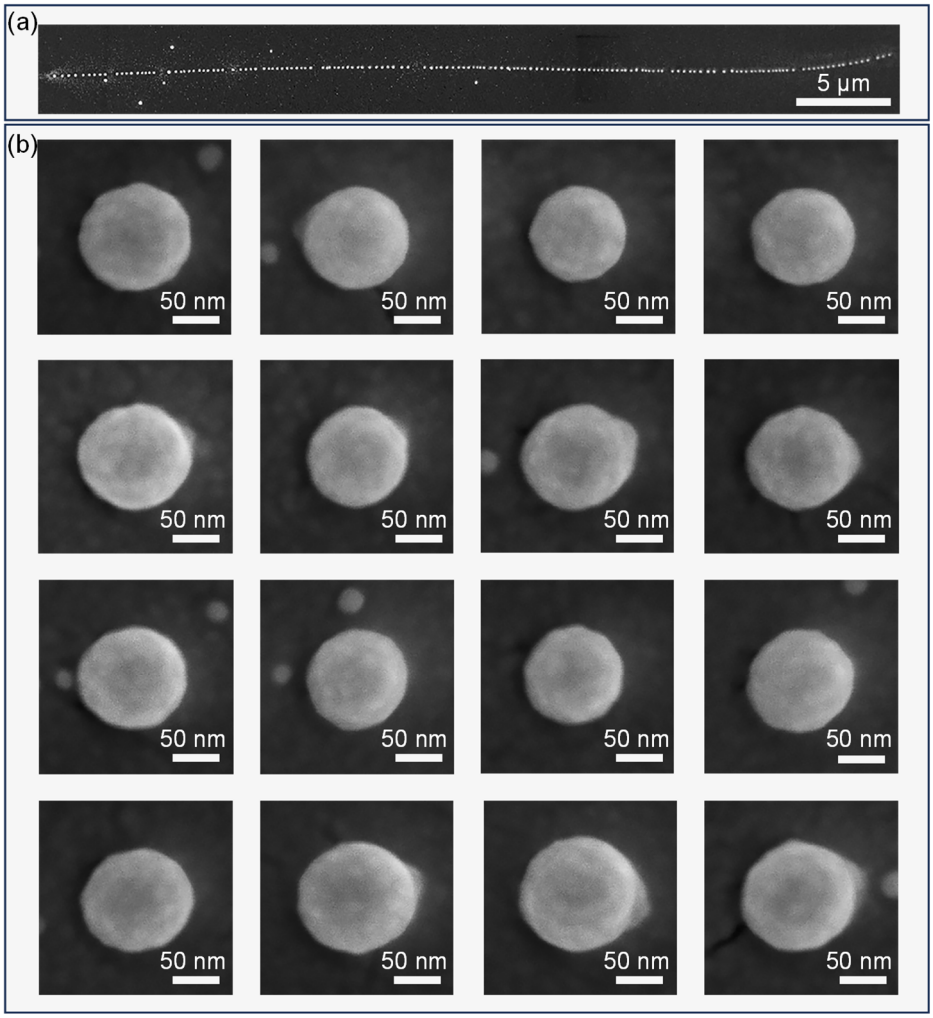

Fig. S2. (a) SEM image of a NP array generated by laser-driven self-organization. (b) High-magnification SEM images of individual NPs in the array in (a).

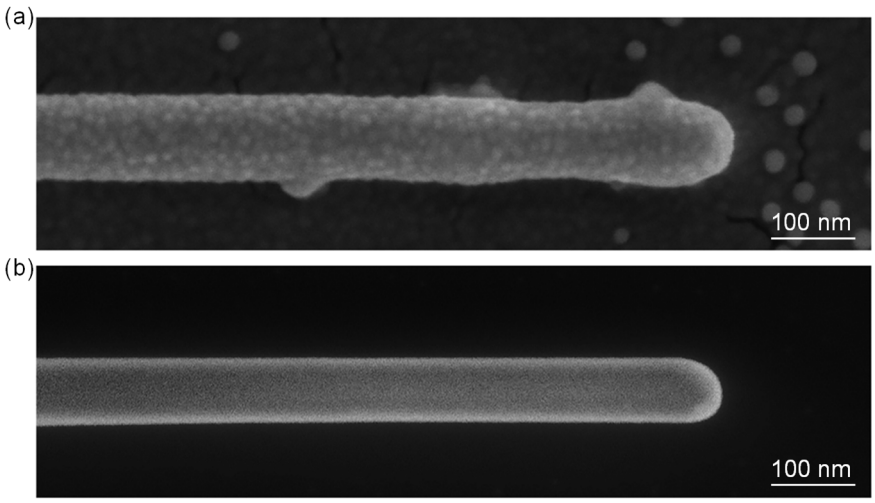

Fig. S3. (a) SEM image of a Ag NW on the same prism substrate under the same Au sputtering coating, but without laser irradiation. (b) SEM image of a Ag NW on a silicon substrate without Au sputtering.

7. Oxidation of Ag NPs in the arrays

Since the Ag NP arrays demonstrated in main text were fabricated on silica (SiO_2) prisms or microfibers, which comprise oxygen element already in the substrates, it would be difficult to characterize the oxidation of Ag NPs on them. To solve this issue, we fabricated Ag NP arrays on a CaF_2 prism (Fig. S4a), using the same laser ablation parameters with the ones on silica prisms. Afterwards, a conductive Au film was deposited on the CaF_2 prism via sputter coating. Then Energy Dispersive X-ray Spectroscopy (EDS) analysis was performed in conjunction with SEM to identify and quantify the elemental composition of the sample. Fig. S4b-d show the EDS spectra of the NPs in the array, and Fig. S4e shows the EDS spectrum of the substrate for comparison. It can be seen that, besides the elements (Ca, F, Au, C) from the substrates, Au sputtering process, or the organic residues, only the Ag-element peak dominates in the EDS spectra for the NPs with negligible O-element peak, indicating that as-fabricated NP arrays are free from obvious signs of oxidation.

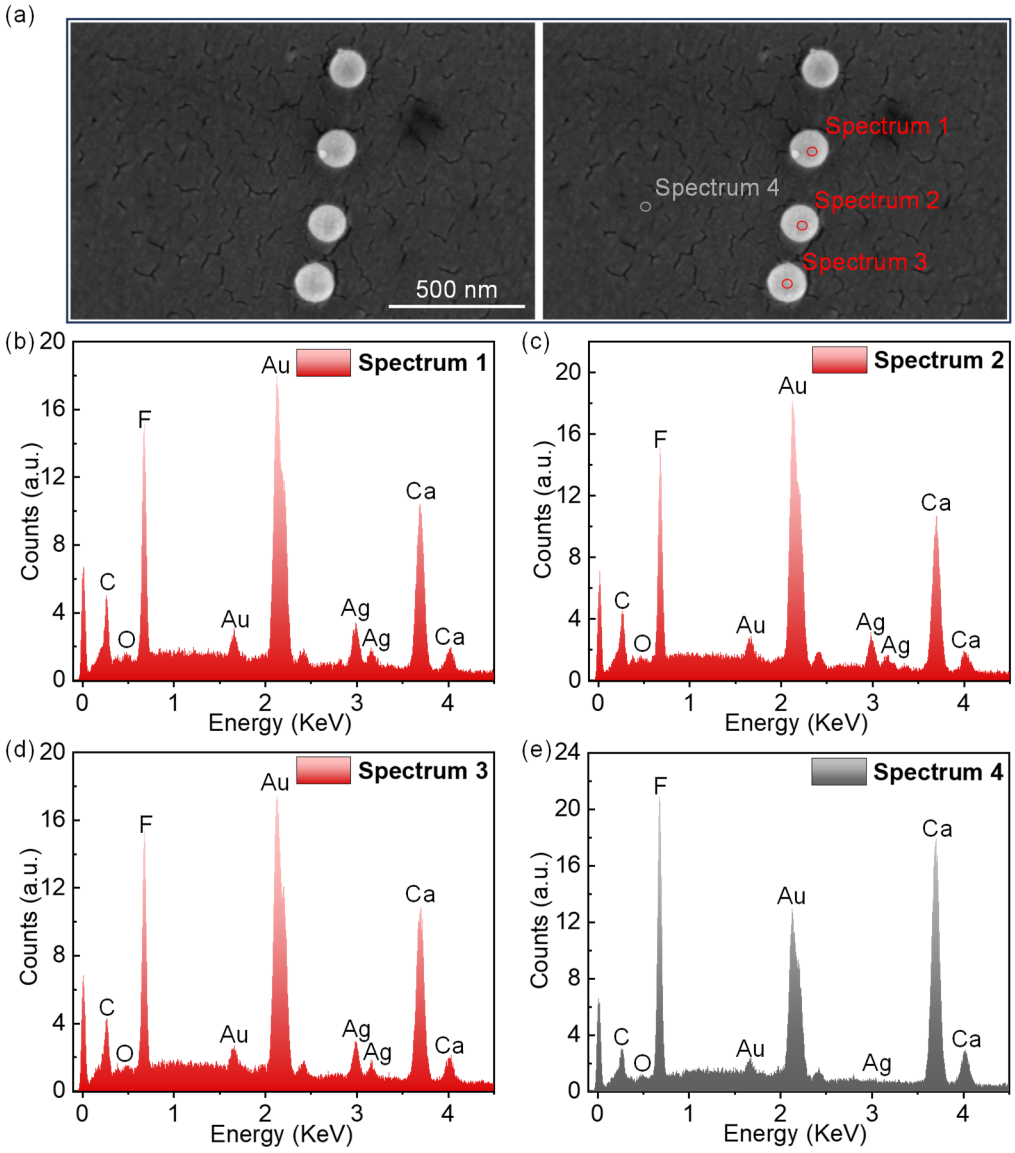

Fig. S4. (a) SEM image of the NP array fabricated on a CaF_2 prism. (b-d) EDS spectra of the Ag NPs collected from the points marked as Spectrum 1-3 in (a), respectively. (e) EDS spectra of the substrate as a background collected from the point marked as Spectrum 4 in (a).

8. Pure thermal decomposition of Ag NWs

To compare our laser ablation method with the pure thermal decomposition, a series of heat-treatment experiments were performed on Ag NWs to investigate their morphological changes under different heating temperatures (T). Specifically, we deposited Ag NWs on a glass substrate, which consists of the same material as the silica prism used in our studies in the main text. Then the glass substrate was placed on a hot plate and heated at 250, 300, 350, 400, and 450 °C under atmospheric conditions for 15 minutes, respectively. Fig. S5 shows the in-situ microscope and SEM images of the morphological evolution as T increases from 250 to 450 °C. As shown in Fig. S5a, when T was below the melting point (i.e., 350 °C as reported in ref. [7,8]), no significant change in the shape of the Ag NWs was observed (Fig. S5a (ii-iii)) compared to the room temperature case (Fig. S5b (i)). As T increased to 350 °C, decomposition of NWs into short fragments or NPs happened, but there was no obvious period of the fragments. When T increased to 400 or 450 °C (Fig. S5b (ii-iii)), the NWs completely disappeared, leaving only some organic residues behind, which is probably due to the evaporation of Ag atoms at high temperatures.

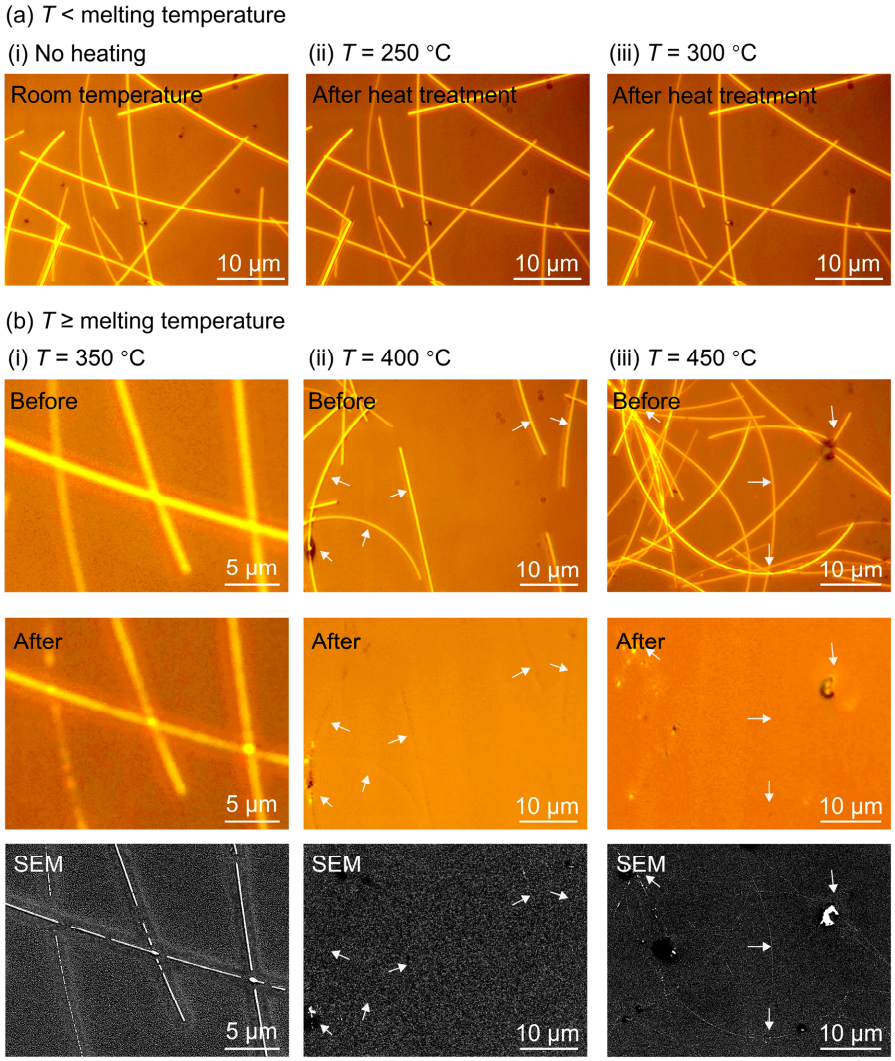

Fig. S5. (a) In-situ microscope images of Ag NWs on a silica substrate before (i) and after heat treatment at T = 250 °C (ii) and 300 °C (iii), respectively. (b) In-situ images of Ag NWs before (top) and after heat treatment (middle: microscope images; bottom: SEM images) at T = 350 °C (i), 400 °C (ii), and 450 °C (iii), respectively.

Since the thermal decomposition of metal NWs is mainly driven by capillary forces and surface diffusion, the crystalline structure may influence the melting behaviors [9]. Therefore, heat-treatment experiments were also performed on Ag NWs on a single-crystalline silicon (Si) substrate. As shown in Fig. S6a, at T = 350 °C, necking and splitting of the NWs are observed, which is similar as the silica substrate. As T increased to 400 or 450 °C, extensive fragmentation of NWs into NPs can be observed, while most of them did not exhibit good periodicity. Few of the NP arrays show a certain degree of periodicity, but the periods are on the micrometer level. Moreover, the NP sizes in the array exhibit considerable large variation.

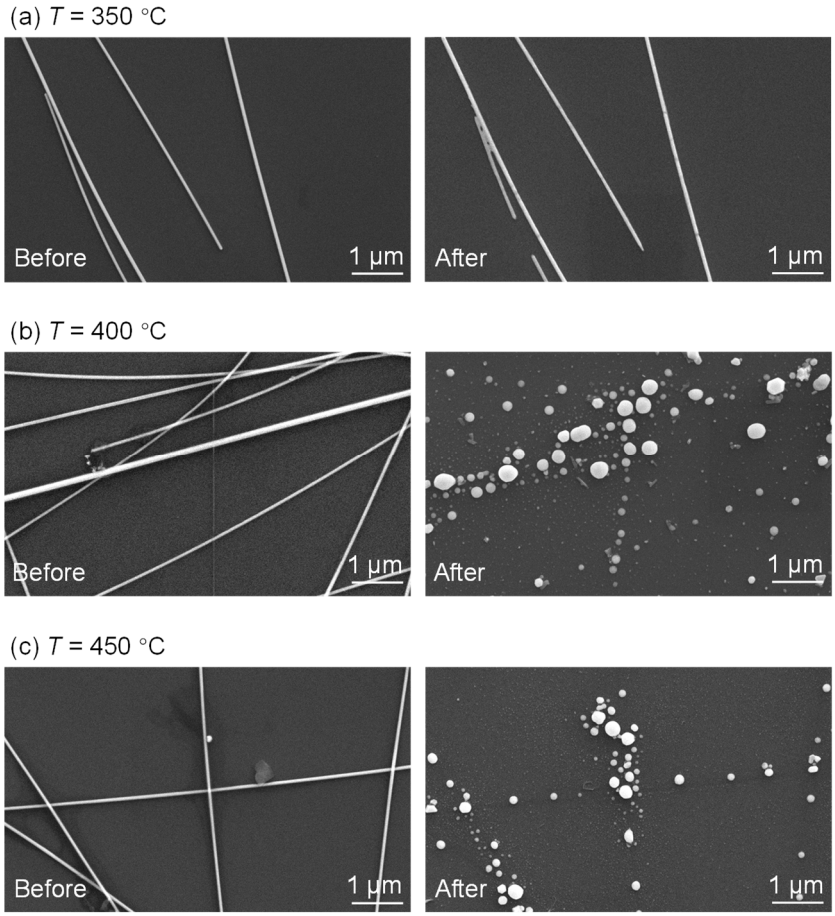

Fig. S6. (a-c) In-situ SEM images of Ag NWs on a silicon substrate before (left) and after (right) heat treatment at T = 350 °C (a), 400 °C (b), and 450 °C (c), respectively.

References

1. Lu, H. M. et al. Size-, Shape-, and Dimensionality-Dependent Melting Temperatures of Nanocrystals. *The Journal of Physical Chemistry C* **113**, 7598–7602 (2009).
2. Rawat, K. & Goyal, M. Thermal conductivity dependence on shape and size in nanomaterials. *Materials Today* **81**, 1132–1137 (2023).
3. Remadevi, A. et al. Electrical, thermal and microwave shielding properties of printable silver nanowires. *Journal of Materials Science* **56**, 15971–15984 (2021).
4. Termentzidis, K. et al. Thermal conductivity and thermal boundary resistance of nanostructures. *Nanoscale Research Letters* **6**, 288 (2011).

5. Chen, X. et al. Nanosecond Photothermal Effects in Plasmonic Nanostructures. *ACS Nano* **6**, 2550–2557 (2012).
6. Sugioka, K. et al. (eds) Handbook of Laser Micro- and Nano-Engineering (Springer International Publishing, 2021).
7. Kim, C.-L. et al. Mechanism of Heat-Induced Fusion of Silver Nanowires. *Scientific Reports* **10**, 9271 (2020).
8. Damerchi, E. et al. Heat-induced morphological changes in silver nanowires deposited on a patterned silicon substrate. *Beilstein Journal of Nanotechnology* **15**, 435–446 (2024).
9. Karim, S. et al. Influence of crystallinity on the Rayleigh instability of gold nanowires*. *Journal of Physics D: Applied Physics* **40**, 3767 (2007).